Toward more complete magnetic gradiometry with the Swarm mission

Kotsiaros, Stavros

Published in:
Earth, Planets and Space

Link to article, DOI:
10.1186/s40623-016-0498-x

Publication date:
2016

Document Version
Publisher's PDF, also known as Version of record

Kotsiaros *Earth, Planets and Space* (2016) 68:130
DOI 10.1186/s40623-016-0498-x

Earth, Planets and Space

FULL PAPER Open Access

Toward more complete magnetic gradiometry with the Swarm mission

Stavros Kotsiaros*

Abstract

An analytical and numerical analysis of the spectral properties of the gradient tensor, initially performed by Rummel and van Gelderen (Geophys J Int 111(1):159–169, 1992) for the gravity potential, shows that when the tensor elements are grouped into sets of semi-tangential and pure-tangential parts, they produce almost identical signal content as the normal element. Moreover, simple eigenvalue relations can be derived between these sets and the spherical harmonic expansion of the potential. This theoretical development generally applies to any potential field. First, the analysis of Rummel and van Gelderen (1992) is adapted to the magnetic field case and then the elements of the magnetic gradient tensor are estimated by 2 years of Swarm data and grouped into $\mathbf{\Gamma}^{(1)} = \{[\nabla \mathbf{B}]_{r\theta}, [\nabla \mathbf{B}]_{r\varphi}\}$ resp. $\mathbf{\Gamma}^{(2)} = \{[\nabla \mathbf{B}]_{\theta\theta} - [\nabla \mathbf{B}]_{\varphi\varphi}, 2[\nabla \mathbf{B}]_{\theta\varphi}\}$. It is shown that the estimated combinations $\mathbf{\Gamma}^{(1)}$ and $\mathbf{\Gamma}^{(2)}$ produce similar signal content as the theoretical radial gradient $\mathbf{\Gamma}^{(0)} = \{[\nabla \mathbf{B}]_{rr}\}$. These results demonstrate the ability of multi-satellite missions such as Swarm, which cannot directly measure the radial gradient, to retrieve similar signal content by means of the horizontal gradients. Finally, lithospheric field models are derived using the gradient combinations $\mathbf{\Gamma}^{(1)}$ and $\mathbf{\Gamma}^{(2)}$ and compared with models derived from traditional vector and gradient data. The model resulting from $\mathbf{\Gamma}^{(1)}$ leads to a very similar, and in particular cases improved, model compared to models retrieved by using approximately three times more data, i.e., a full set of vector, North–South and East–West gradients. This demonstrates the high information content of $\mathbf{\Gamma}^{(1)}$.

Keywords: Crustal field, Swarm gradients, Field modeling

Introduction

The Earth possesses an intrinsic magnetic field, the major part of which is produced by a self-sustaining dynamo operating in the outer core. However, what is measured at or near the Earth's surface is a superposition of the core field, the lithospheric field due to magnetized rocks in the Earth's lithosphere, external fields caused by electric currents in the ionosphere and the magnetosphere, and fields due to currents induced in the Earth by the time-varying external fields. More than 14 years of satellite measurements from Ørsted (Neubert et al. 2001) and CHAMP (Reigber et al. 2005) led to detailed and precise models of Earth's magnetic field. The Swarm satellite mission (Friis-Christensen et al. 2006) was launched by the European Space Agency (ESA) on November 22, 2013, and is the first multi-satellite mission dedicated to the geomagnetic field exploration from space. Specifically, it consists of three identical spacecrafts two of which are flying side-by-side at lower altitudes (roughly at 450 km initial altitude) separated in longitude by 1.4°, which allows for an instantaneous estimation of the East–West gradient of the magnetic field. The third flies at higher altitude (530 km) and at different local time compared to the lower pair. Kotsiaros et al. (2015) have recently showed that North–South gradients can be approximated by first differences along the orbit track and a model of the Earth's magnetic field based on East–West and North–South gradients estimated from Swarm data differences has already been presented by Olsen et al. (2015).

On the other hand, Swarm with its current configuration is unable to directly estimate the radial gradient since this would require two satellites separated along the radial direction. However, the radial gradient seems

*Correspondence: skotsiaros@space.dtu.dk
Division of Geomagnetism, DTU Space, Techincal University of Denmark, Diplomvej 371, Kgs. Lyngby, Denmark

to provide the highest information content (Kotsiaros and Olsen 2012) and could therefore be important for improving existing magnetic field models. In order to overcome this limitation of Swarm, we translate a tensorial analysis originally developed for the gravity field by Rummel and van Gelderen (1992) to the magnetic field case which shows that specific combinations of East–West and North–South gradients provide a similar signal content to the radial gradient. Thus, radial gradient information can indirectly be inferred using the Swarm constellation and therefore additional information on primarily the lithospheric field could possibly be extracted.

Tensor harmonics

The scalar potential V for internal magnetic field sources can be written as

$$V = \mathbb{R}\left\{ a \sum_{n=1}^{N} \sum_{m=0}^{n} \gamma_n^m \left(\frac{a}{r}\right)^{n+1} Y_{nm} \right\}, \tag{1}$$

where $\mathbb{R} = \{\dots\}$ denotes the real part of the series, the scaling factor $a = 6371.2$ km is the Earth's mean radius, $\gamma_n^m = g_n^m - ih_n^m$ are the complex spherical harmonic expansion coefficients describing the internal sources and $Y_{nm} = \exp(im\varphi) P_n^m(\cos\theta)$ the surface spherical harmonics, (r, θ, φ) the geocentric spherical coordinates and $P_n^m(\cos\theta)$ the associated Schmidt semi-normalized Legendre functions of degree n and order m. Following Kotsiaros and Olsen (2012), the magnetic field gradient tensor elements can be written as

$$[\nabla \mathbf{B}]_{jk} = \mathbb{R}\left\{ \frac{1}{a} \sum_{n=1}^{N} \sum_{m=0}^{n} \gamma_n^m \left(\frac{a}{r}\right)^{n+3} Y_{nm}^{jk} \right\}, \tag{2}$$

where the first subscript, j, stands for the vector component for which the derivative is taken, while the second subscript, k, indicates the direction of the spatial derivative, with $j, k = r, \theta, \varphi$, whereas the functions Y_{nm}^{jk} are given by

$$Y_{nm}^{rr} = -(n+1)(n+2)\exp(im\varphi) P_n^m(\cos\theta), \tag{3}$$

$$Y_{nm}^{\theta\theta} = \exp(im\varphi)\left[(n+1) P_n^m(\cos\theta) - \frac{d^2 P_n^m(\cos\theta)}{d\theta^2} \right], \tag{4}$$

$$Y_{nm}^{\varphi\varphi} = \exp(im\varphi)\left[\left(\frac{m^2}{\sin^2\theta} + (n+1) \right) P_n^m(\cos\theta) - \cot\theta \frac{dP_n^m(\cos\theta)}{d\theta} \right], \tag{5}$$

$$Y_{nm}^{r\theta} = \exp(im\varphi)(n+2)\frac{dP_n^m(\cos\theta)}{d\theta}, \tag{6}$$

$$Y_{nm}^{r\varphi} = \exp(im\varphi)\frac{m(n+2)}{\sin\theta} i P_n^m(\cos\theta), \tag{7}$$

$$Y_{nm}^{\theta\varphi} = \exp(im\varphi)\left[\frac{m\cos\theta}{\sin^2\theta} i P_n^m(\cos\theta) - \frac{m}{\sin\theta} i \frac{dP_n^m(\cos\theta)}{d\theta} \right]. \tag{8}$$

According to Rummel and van Gelderen (1992), the three tensor observables $\mathbf{\Gamma}^{(0)} = \{[\nabla \mathbf{B}]_{rr}\}$, $\mathbf{\Gamma}^{(1)} = \{[\nabla \mathbf{B}]_{r\theta}, [\nabla \mathbf{B}]_{r\varphi}\}$ and $\mathbf{\Gamma}^{(2)} = \{[\nabla \mathbf{B}]_{\theta\theta} - [\nabla \mathbf{B}]_{\varphi\varphi}, 2[\nabla \mathbf{B}]_{\theta\varphi}\}$ are represented by three tensor spherical harmonics denoted $\mathbf{Z}_{nm}^{(0)}$, $\mathbf{Z}_{nm}^{(1)}$ and $\mathbf{Z}_{nm}^{(2)}$. These tensor spherical harmonics are orthogonal and particularly

$$\int_0^{2\pi} \int_0^{\pi} \sum_{j,k} \left[\mathbf{Z}_{nm}^{(\alpha)}\right]_{jk} \left[\mathbf{Z}_{n'm'}^{(\beta)}\right]_{jk} \sin\theta d\theta d\varphi = \frac{4\pi}{2n+1} \delta_{nn'} \delta_{mm'} \delta_{\alpha\beta} \tag{9}$$

where $\alpha, \beta = \{0, 1, 2\}$, $[\ ]_{jk}$ denote the tensor components and $\delta_{nn'}$, $\delta_{mm'}$, $\delta_{\alpha\beta}$ are the Kronecker delta. With $\psi_{nm} = \left(\frac{a}{r}\right)^{n+1} Y_{nm}$ the spatial spherical harmonics, the tensor spherical harmonics are defined by the following eigenvalue expansions:

$$a^2 \mathcal{L}^{(0)} \psi_{nm} = a^2 \begin{pmatrix} \frac{\partial^2}{\partial r^2} & 0 & 0 \\ 0 & 0 & 0 \\ 0 & 0 & 0 \end{pmatrix} \psi_{nm} = \left(\frac{a}{r}\right)^{(n+3)} (n+1)(n+2) \mathbf{Z}_{nm}^{(0)}, \tag{10}$$

$$\text{with} \quad \mathbf{Z}_{nm}^{(0)} \equiv \begin{pmatrix} Y_{nm} & 0 & 0 \\ 0 & 0 & 0 \\ 0 & 0 & 0 \end{pmatrix} \tag{11}$$

$$a^2 \mathcal{L}^{(1)} \psi_{nm} = \frac{a^2}{\sqrt{2}} \begin{pmatrix} 0 & \frac{1}{r}\frac{\partial^2}{\partial\theta\partial r} - \frac{1}{r^2}\frac{\partial}{\partial\theta} & \frac{1}{r\sin\theta}\frac{\partial^2}{\partial\varphi\partial r} - \frac{1}{r^2\sin\theta}\frac{\partial}{\partial\varphi} \\ \star & 0 & 0 \\ \star & 0 & 0 \end{pmatrix} \psi_{nm} = -\left(\frac{a}{r}\right)^{(n+3)} (n+2)\sqrt{n(n+1)} \mathbf{Z}_{nm}^{(1)}, \tag{12}$$

$$\text{with} \quad \mathbf{Z}_{nm}^{(1)} \equiv \frac{r\sqrt{2}}{\sqrt{n(n+1)}} \frac{1}{2} \begin{pmatrix} 0 & \frac{1}{r}\frac{\partial Y_{nm}}{\partial\theta} & \frac{1}{r\sin\theta}\frac{\partial Y_{nm}}{\partial\varphi} \\ \star & 0 & 0 \\ \star & 0 & 0 \end{pmatrix} \tag{13}$$

$$a^2\mathcal{L}^{(2)}\psi_{nm} = \frac{a^2}{\sqrt{2}}\begin{pmatrix} 0 & 0 & 0 \\ 0 & \frac{1}{r^2}\frac{\partial^2}{\partial\theta^2} - \frac{\cot\theta}{r^2}\frac{\partial}{\partial\theta} - \frac{1}{r^2\sin^2\theta}\frac{\partial^2}{\partial\varphi^2} & \frac{2}{r^2\sin\theta}\left(\frac{\partial^2}{\partial\theta\partial\varphi} - \cot\theta\frac{\partial}{\partial\varphi}\right) \\ 0 & \star & -\frac{1}{r^2}\frac{\partial^2}{\partial\theta^2} + \frac{\cot\theta}{r^2}\frac{\partial}{\partial\theta} + \frac{1}{r^2\sin^2\theta}\frac{\partial^2}{\partial\varphi^2} \end{pmatrix}\psi_{nm}$$
$$= \left(\frac{a}{r}\right)^{(n+3)}\sqrt{(n-1)n(n+1)(n+2)}\mathbf{Z}^{(2)}_{nm}, \tag{14}$$

$$\text{with } \mathbf{Z}^{(2)}_{nm} \equiv \frac{r^2}{\sqrt{2n(n+1)(n-1)(n+2)}} \times \begin{pmatrix} 0 & 0 & 0 \\ 0 & \frac{1}{r^2}\left[\frac{\partial^2 Y_{nm}}{\partial\theta^2} - \cot\theta\frac{\partial Y_{nm}}{\partial\theta} - \frac{1}{\sin^2\theta}\frac{\partial^2 Y_{nm}}{\partial\varphi^2}\right] & \frac{2}{r^2\sin\theta}\left(\frac{\partial^2 Y_{nm}}{\partial\varphi\partial\theta} - \cot\theta\frac{\partial Y_{nm}}{\partial\varphi}\right) \\ 0 & \star & -\frac{1}{r^2}\left[\frac{\partial^2 Y_{nm}}{\partial\theta^2} - \cot\theta\frac{\partial Y_{nm}}{\partial\theta} - \frac{1}{\sin^2\theta}\frac{\partial^2 Y_{nm}}{\partial\varphi^2}\right] \end{pmatrix}. \tag{15}$$

The $\star$ indicates symmetry of the component with respect to the main diagonal. For more details on the analytical expressions of the operators $\mathcal{L}^{(0)}$, $\mathcal{L}^{(1)}$ and $\mathcal{L}^{(2)}$, the reader is referred to Zerilli (1970), whereas the tensor spherical harmonics $\mathbf{Z}^{(0)}_{nm}$, $\mathbf{Z}^{(1)}_{nm}$ and $\mathbf{Z}^{(2)}_{nm}$ are Zerilli's orthogonal harmonics $\mathbf{a}_{nm}$, $\mathbf{b}_{nm}$ and $\mathbf{f}_{nm}$ respectively, multiplied by a scale factor. A similar basis of tensor spherical harmonics has been derived for the gravity gradient tensor, see, e.g., Meissl (1971), Rummel (1997), Rummel and van Gelderen (1992).

Applying the operators $\mathcal{L}^{(0)}$, $\mathcal{L}^{(1)}$, $\mathcal{L}^{(2)}$, Eqs. (10–14), to the potential V, cf. Eq. (1), gives the expansions of the observables $\mathbf{\Gamma}^{(0)}$, $\mathbf{\Gamma}^{(1)}$ and $\mathbf{\Gamma}^{(2)}$. Specifically,

$$\mathbf{\Gamma}^{(0)} = \mathcal{L}^{(0)}V_{\text{int}} = \mathbb{R}\left\{a\sum_{n=1}^{N}\sum_{m=0}^{n}\gamma_n^m\mathcal{L}^{(0)}\psi_{nm}\right\}$$
$$= \mathbb{R}\left\{\frac{1}{a}\sum_{n=1}^{N}\sum_{m=0}^{n}\gamma_n^m\left(\frac{a}{r}\right)^{(n+3)}(n+1)(n+2)\mathbf{Z}^{(0)}_{nm}\right\}$$
$$= \mathbb{R}\left\{\frac{1}{a}\sum_{n=1}^{N}\sum_{m=0}^{n}\left(\frac{a}{r}\right)^{(n+3)}\zeta^{(0)}_{nm}\mathbf{Z}^{(0)}_{nm}\right\} \tag{16}$$

$$\mathbf{\Gamma}^{(1)} = \mathcal{L}^{(1)}V_{\text{int}} = \mathbb{R}\left\{a\sum_{n=1}^{N}\sum_{m=0}^{n}\gamma_n^m\mathcal{L}^{(1)}\psi_{nm}\right\}$$
$$= \mathbb{R}\left\{-\frac{1}{a}\sum_{n=1}^{N}\sum_{m=0}^{n}\gamma_n^m\left(\frac{a}{r}\right)^{(n+3)}(n+2)\sqrt{n(n+1)}\mathbf{Z}^{(1)}_{nm}\right\}$$
$$= \mathbb{R}\left\{\frac{1}{a}\sum_{n=1}^{N}\sum_{m=0}^{n}\left(\frac{a}{r}\right)^{(n+3)}\zeta^{(1)}_{nm}\mathbf{Z}^{(1)}_{nm}\right\} \tag{17}$$

$$\mathbf{\Gamma}^{(2)} = \mathcal{L}^{(2)}V_{\text{int}} = \mathbb{R}\left\{a\sum_{n=1}^{N}\sum_{m=0}^{n}\gamma_n^m\mathcal{L}^{(2)}\psi_{nm}\right\}$$
$$= \mathbb{R}\left\{\frac{1}{a}\sum_{n=1}^{N}\sum_{m=0}^{n}\gamma_n^m\left(\frac{a}{r}\right)^{(n+3)}\sqrt{(n-1)n(n+1)(n+2)}\mathbf{Z}^{(2)}_{nm}\right\}$$
$$= \mathbb{R}\left\{\frac{1}{a}\sum_{n=1}^{N}\sum_{m=0}^{n}\left(\frac{a}{r}\right)^{(n+3)}\zeta^{(2)}_{nm}\mathbf{Z}^{(2)}_{nm}\right\}. \tag{18}$$

The expansion coefficients $\zeta^{(0)}_{nm}$, $\zeta^{(1)}_{nm}$ and $\zeta^{(2)}_{nm}$ of the three tensor observables $\mathbf{\Gamma}^{(0)}$, $\mathbf{\Gamma}^{(1)}$ and $\mathbf{\Gamma}^{(2)}$ are associated with the coefficients γ_n^m of the potential V with the following eigenvalue relations

$$\zeta^{(0)}_{nm} = (n+1)(n+2)\gamma_n^m, \tag{19}$$

$$\zeta^{(1)}_{nm} = -(n+2)\sqrt{n(n+1)}\gamma_n^m, \tag{20}$$

$$\zeta^{(2)}_{nm} = \sqrt{(n-1)n(n+1)(n+2)}\gamma_n^m. \tag{21}$$

Notice that the three types of observables are related to the magnetic potential V with a factor of n^2, whereas if the magnetic potential is to be determined only by the observable $\mathbf{\Gamma}^{(2)}$, singularity emerges for degree $n = 1$.

Spectral analysis

A similar spectrum to the Mauersberger–Lowes spectrum (Backus et al. 1996; Lowes 1974) can be calculated for the three different observables $\mathbf{\Gamma}^{(0)}$, $\mathbf{\Gamma}^{(1)}$ and $\mathbf{\Gamma}^{(2)}$ as

$$R_n^{(\beta)}(r) = \frac{1}{4\pi r^2}\int_\Omega \sum_{j,k}\left[\mathbf{\Gamma}_n^{(\beta)}\right]_{jk}\left[\mathbf{\Gamma}_n^{(\beta)}\right]_{jk} d\Omega \tag{22}$$

where $\beta = \{0,1,2\}$, $[\,]_{jk}$ stands for the tensor components and $d\Omega = r^2\sin\theta d\theta d\phi$. Based on Eqs. 16, 17 and 18, the eigenvalue relations 19, 20 and 21 as well as the orthogonality of the tensor spherical harmonics, Eq. 9, we get

$$R_n^{(0)}(r) = \frac{1}{a^2}\left(\frac{a}{r}\right)^{(2n+6)}\frac{[(n+1)(n+2)]^2}{2n+1}\sum_{m=1}^{n}||\gamma_n^m||^2, \tag{23}$$

$$R_n^{(1)}(r) = \frac{1}{a^2}\left(\frac{a}{r}\right)^{(2n+6)}\frac{(n+2)^2 n(n+1)}{2n+1}\sum_{m=1}^{n}||\gamma_n^m||^2, \tag{24}$$

$$R_n^{(2)}(r) = \frac{1}{a^2}\left(\frac{a}{r}\right)^{(2n+6)}\frac{(n-1)n(n+1)(n+2)}{2n+1}\sum_{m=1}^{n}||\gamma_n^m||^2. \tag{25}$$

Figure 1 shows the spectra $R_n^{(0)}(r_h)$, $R_n^{(1)}(r_h)$ and $R_n^{(2)}(r_h)$ of the observables $\mathbf{\Gamma}^{(0)}$, $\mathbf{\Gamma}^{(1)}$ and $\mathbf{\Gamma}^{(2)}$, respectively, at $r = r_h = a + h$, where $h = 0$ km (dashed lines) and $h = 460$ km (solid lines). The coefficients γ_n^m are taken from the MF7[1] model by Maus et al. (2008). One observes the slightly higher power of $\mathbf{\Gamma}^{(0)}$ and the slightly weaker power of $\mathbf{\Gamma}^{(2)}$; however, it can be seen that $\mathbf{\Gamma}^{(0)}$, $\mathbf{\Gamma}^{(1)}$ and $\mathbf{\Gamma}^{(2)}$ share in general almost identical spectral levels.

A detailed spectral analysis of the full magnetic gradient tensor has been done by Kotsiaros and Olsen (2012). The analysis was based on obtaining the variances σ of the estimated model parameters for each gradient tensor element independently, with

$$\sigma^2 = \sigma_d^2\left[\mathrm{diag}\{(\mathbf{G}^T\mathbf{G})^{-1}\}\right]. \tag{26}$$

σ_d^2 is the variance of independent observations and $\mathbf{G}$ the kernel matrix relating the model vector $\mathbf{m}$, containing the unknown spherical harmonic coefficients γ_n^m, to the data vector $\mathbf{d}$, containing observations of the vector component or gradient elements, such that $\mathbf{d} = \mathbf{G}\mathbf{m}$. An analytical expression of σ is possible to be derived for the tensor element $[\nabla\mathbf{B}]_{rr}$, i.e., the observable $\mathbf{\Gamma}^{(0)}$. Despite the fact that for the remaining individual tensor elements orthogonality cannot be assumed and their spectral behavior cannot be expressed analytically, e.g., Groten et al. (1964), van Gelderen and Koop (1997), analytical expressions can be derived for $\mathbf{\Gamma}^{(1)}$ and $\mathbf{\Gamma}^{(2)}$, which consist of specific combinations of tensor elements, i.e., $\{[\nabla\mathbf{B}]_{r\theta}, [\nabla\mathbf{B}]]_{r\varphi}\}$ and $\{[\nabla\mathbf{B}]_{\theta\theta} - [\nabla\mathbf{B}]_{\varphi\ varphi}, 2[\nabla\mathbf{B}]_{\theta\varphi}\}$, respectively. This is possible because $\mathbf{\Gamma}^{(0)}$, $\mathbf{\Gamma}^{(1)}$ and $\mathbf{\Gamma}^{(2)}$ can be directly represented in terms of a complete orthonormal system of tensor spherical harmonics, cf. Eqs. (16), (17) and (18).

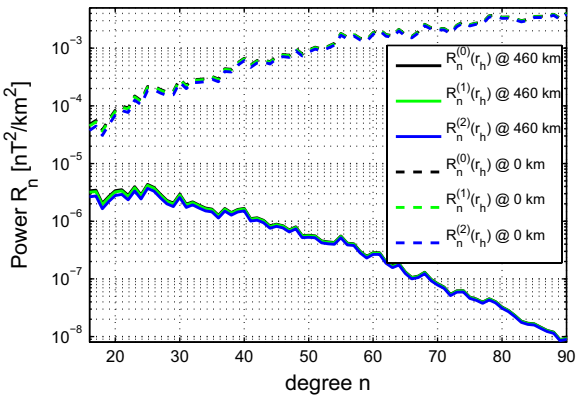

Fig. 1 Power spectra $R_n^{(0)}(r_h)$, $R_n^{(1)}(r_h)$ and $R_n^{(2)}(r_h)$ of the observables $\mathbf{\Gamma}^{(0)}$, $\mathbf{\Gamma}^{(1)}$ and $\mathbf{\Gamma}^{(2)}$ at the Earth's surface, $h = 0$ km, (*dashed lines*) and at $h = 460$ km altitude (*solid lines*) based on MF7 model

Following Lowes (1966) or Langel (1987), for the case that the observations consist of N_d measurements of $\mathbf{\Gamma}^{(0)}$, i.e., $\mathbf{d} = \{[\nabla\mathbf{B}]_{rr}\}$, the $\mathbf{G}^T\mathbf{G}$ can be approximated by

$$\begin{aligned}\mathbf{G}^T\mathbf{G} \approx & \frac{N_d}{4\pi a^2}\int_0^{2\pi}\int_0^{\pi}(n+1)\\ & \times (n+2)(n'+1)(n'+2)\left(\frac{a}{r}\right)^{(n+3)}\left(\frac{a}{r}\right)^{(n'+3)}\\ & \times \mathbf{Z}_{nm}^{(0)}\mathbf{Z}_{n'm'}^{(0)}\sin\theta d\theta d\varphi\\ = & \frac{1}{a^2}\left(\frac{a}{r}\right)^{(2n+6)}\frac{N_d[(n+1)(n+2)]^2}{2n+1}\delta_{m,m'}\delta_{n,n'},\end{aligned} \tag{27}$$

due to orthogonality of the tensor spherical harmonics, cf. Eq. (9). Therefore, the variances of the estimated model parameters are

$$\sigma_{(0)}^2 \approx (a\sigma_d)^2\left(\frac{r}{a}\right)^{(2n+6)}\frac{2n+1}{N_d[(n+1)(n+2)]^2}, \quad \text{if } \mathbf{d} = \{[\nabla\boldsymbol{B}]_{rr}\}. \tag{28}$$

Respectively, when the observations consist of N_d measurements of $\mathbf{\Gamma}^{(1)}$, i.e., $\mathbf{d} = \{[\nabla\mathbf{B}]_{r\theta}, [\nabla\mathbf{B}]_{r\varphi}\}$, the $\mathbf{G}^T\mathbf{G}$ reads

$$\begin{aligned}\mathbf{G}^T\mathbf{G} \approx & \frac{N_d}{4\pi a^2}\int_0^{2\pi}\int_0^{\pi}[(n+2)\sqrt{n(n+1)}]\\ & \times [(n'+2)\sqrt{n'(n'+1)}]\left(\frac{a}{r}\right)^{(n+3)}\\ & \times \left(\frac{a}{r}\right)^{(n'+3)}\mathbf{Z}_{nm}^{(1)}\mathbf{Z}_{n'm'}^{(1)}\sin\theta d\theta d\varphi\\ = & \frac{1}{a^2}\left(\frac{a}{r}\right)^{(2n+6)}\frac{N_d[(n+2)^2 n(n+1)]}{2n+1}\delta_{m,m'}\delta_{n,n'}.\end{aligned} \tag{29}$$

[1] http://www.geomag.org/models/MF7.html.

Therefore, the variances of the estimated model parameters are

$$\sigma^2_{(1)} \approx (a\sigma_d)^2 \left(\frac{r}{a}\right)^{(2n+6)} \frac{2n+1}{N_d[(n+2)^2 n(n+1)]}, \quad \text{if } \mathbf{d} = \{[\nabla \mathbf{B}]_{r\theta}, [\nabla \mathbf{B}]_{r\varphi}\}. \tag{30}$$

Finally, when the observations consist of N_d measurements of $\mathbf{\Gamma}^{(2)}$, i.e., $\mathbf{d} = \{[\nabla \mathbf{B}]_{\theta\theta} - [\nabla \mathbf{B}]_{\varphi\varphi}, 2[\nabla \mathbf{B}]_{\theta\varphi}\}$, the $\mathbf{G}^T\mathbf{G}$ is given by

$$\begin{aligned} \mathbf{G}^T\mathbf{G} &\approx \frac{N_d}{4\pi a^2} \int_0^{2\pi} \int_0^{\pi} \sqrt{(n-1)n(n+1)(n+2)} \\ &\quad \times \sqrt{(n'-1)n'(n'+1)(n'+2)} \\ &\quad \times \left(\frac{a}{r}\right)^{(n+3)} \left(\frac{a}{r}\right)^{(n'+3)} \mathbf{Z}^{(2)}_{nm} \mathbf{Z}^{(2)}_{n'm'} \sin\theta d\theta d\varphi \\ &= \frac{1}{a^2} \left(\frac{a}{r}\right)^{(2n+6)} \frac{N_d[(n-1)n(n+1)(n+2)]}{2n+1} \delta_{m,m'} \delta_{n,n'}. \end{aligned} \tag{31}$$

Therefore, the variances of the estimated model parameters are

$$\sigma^2_{(2)} \approx (a\sigma_d)^2 \left(\frac{r}{a}\right)^{(2n+6)} \frac{2n+1}{N_d[(n-1)n(n+1)(n+2)]}, \quad \text{if } \mathbf{d} = \{[\nabla \mathbf{B}]_{\theta\theta} - [\nabla \mathbf{B}]_{\varphi\varphi}, 2[\nabla \mathbf{B}]_{\theta\varphi}\}. \tag{32}$$

The variances $\sigma^2_{(0)}$, $\sigma^2_{(1)}$ and $\sigma^2_{(2)}$ which are obtained when observations consist of $\mathbf{\Gamma}^{(0)}$, $\mathbf{\Gamma}^{(1)}$ and $\mathbf{\Gamma}^{(2)}$, respectively, are almost identical and are proportional to a factor of $\frac{1}{n^3}$. If the model parameters are estimated by the observable $\mathbf{\Gamma}^{(2)}$, singularity emerges for degree $n = 1$, which was also pointed out by its eigenvalue Eq. (21). The analytically calculated model variances a) $\sigma^2_{(0)}$, b) $\sigma^2_{(1)}$ and c) $\sigma^2_{(2)}$, cf. Eqs. (28), (30) and (32), are shown in Fig. 2 in dependence of degree n and order m. White represents high variance, i.e., low information content, whereas green represents low variance, i.e., high information content. One can see that the specific combinations $\{[\nabla \mathbf{B}]_{r\theta}, [\nabla \mathbf{B}]_{r\varphi}\}$ and $\{[\nabla \mathbf{B}]_{\theta\theta} - [\nabla \mathbf{B}]_{\varphi\varphi}, 2[\nabla \mathbf{B}]_{\theta\varphi}\}$, namely $\mathbf{\Gamma}^{(1)}$ resp. $\mathbf{\Gamma}^{(2)}$, which basically are combinations of North–South and East–West gradients, have in theory almost identical information content as the radial gradient $[\nabla \mathbf{B}]_{rr}$, i.e., the observable $\mathbf{\Gamma}^{(0)}$. For that reason and for simplicity, we refer to $\mathbf{\Gamma}^{(1)}$ and $\mathbf{\Gamma}^{(2)}$ as pseudo-radial gradients.

In the next section, I try to identify whether this conclusion could have a practical use in the Swarm case, e.g., can we make use of the North–South and East–West gradient combinations to get similar information as the radial gradient which is not measured by the Swarm constellation? To facilitate this, the observables $\mathbf{\Gamma}^{(1)}$ and $\mathbf{\Gamma}^{(2)}$ are estimated from Swarm data and their information content (regarding the recovery of the model parameters) is tested against the content of the theoretical radial gradient $\mathbf{\Gamma}^{(0)}$. Subsequently, lithospheric field models are derived using the observables $\mathbf{\Gamma}^{(1)}$ and $\mathbf{\Gamma}^{(2)}$, which are estimated from Swarm data.

Lithospheric field modeling with Swarm pseudo-radial gradients

Data form Swarm Alpha and Charlie have been selected during 23 months, between April 2014 and March 2016,

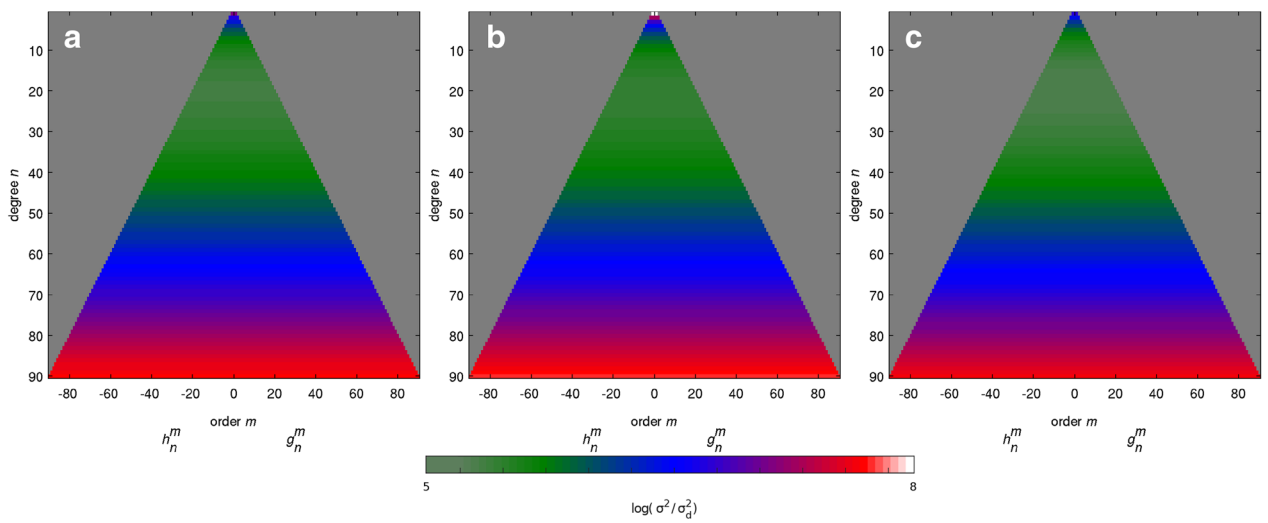

Fig. 2 Variance at satellite altitude ($r = a + 460$ km) of the estimated model parameters from each observable **a** $\mathbf{\Gamma}^{(1)}$, **b** $\mathbf{\Gamma}^{(2)}$ and **c** $\mathbf{\Gamma}^{(0)}$, based on their analytical expressions, Eqs. (28), (30) and (32), respectively. *White* represents low information content, whereas *green* represents high information content

with a sampling rate of 15 seconds. To derive a lithospheric field model, predictions from CHAOS-6 (Finlay et al. 2016) for both the core field (up to spherical harmonic degree $N = 15$) and the large-scale magnetospheric field are subtracted from the vector data. Known disturbed days, for example associated with satellite maneuvers, are excluded. In addition, outliers for which the vector components exceed 300 nT the CHAOS-6 model predictions are removed. Due to the failure of both absolute scalar magnetometers on Swarm Charlie after November 2014, its vector magnetometer is calibrated using scalar field values mapped over from Swarm Alpha. Moreover, vector field data are selected from dark regions (sun at least 10° below the horizon) and during relatively quiet geomagnetic conditions such as the change in the RC-index $\leq$3 nT/h and $K_p \leq 3°$. For quasi-dipole (QD), Richmond (1995), latitudes polewards of $\pm 55°$ the horizontal vector components are excluded. Based on these data, the individual gradient elements $[\nabla \mathbf{B}]_{jk}$, with $j,k = r,\theta,\varphi$, which make up the observables $\mathbf{\Gamma}^{(1)} = \{[\nabla \mathbf{B}]]_{r\theta}, [\nabla \mathbf{B}]_{r\varphi}\}$ resp. $\mathbf{\Gamma}^{(2)} = \{[\nabla \mathbf{B}]_{\theta\theta} - [\nabla \mathbf{B}]_{\varphi\varphi}, 2[\nabla \mathbf{B}]_{\theta\varphi}\}$ are estimated. Their expression as elements of the simplified gradient tensor is used, see equation 3.9 of Kotsiaros and Olsen (2012), which holds for small-scale field features, i.e., the lithospheric field. Their calculation is done by means of first-order Taylor expansion. Specifically,

$$[\nabla \mathbf{B}]_{r\theta} \approx \frac{B_r(r_1,\theta_1,\varphi_1) - B_r(r_2,\theta_2,\varphi_2)}{S_{\mathrm{NS}}}, \quad \text{with } \theta_2 - \theta_1 \gg \varphi_2 - \varphi_1, \tag{33}$$

$$[\nabla \mathbf{B}]_{r\varphi} \approx \frac{B_r(r_1,\theta_1,\varphi_1) - B_r(r_2,\theta_2,\varphi_2)}{S_{\mathrm{EW}}}, \quad \text{with } \varphi_2 - \varphi_1 \gg \theta_2 - \theta_1, \tag{34}$$

$$[\nabla \mathbf{B}]_{\theta\theta} \approx \frac{B_\theta(r_1,\theta_1,\varphi_1) - B_\theta(r_2,\theta_2,\varphi_2)}{S_{\mathrm{NS}}}, \quad \text{with } \theta_2 - \theta_1 \gg \varphi_2 - \varphi_1, \tag{35}$$

$$[\nabla \mathbf{B}]_{\varphi\varphi} \approx \frac{B_\varphi(r_1,\theta_1,\varphi_1) - B_\varphi(r_2,\theta_2,\varphi_2)}{S_{\mathrm{EW}}}, \quad \text{with } \varphi_2 - \varphi_1 \gg \theta_2 - \theta_1, \tag{36}$$

$$[\nabla \mathbf{B}]_{\theta\varphi} \approx \frac{B_\theta(r_1,\theta_1,\varphi_1) - B_\theta(r_2,\theta_2,\varphi_2)}{S_{\mathrm{EW}}}, \quad \text{with } \varphi_2 - \varphi_1 \gg \theta_2 - \theta_1. \tag{37}$$

S_{NS} is the North–South spherical distance, i.e., the distance between consecutive positions (along-track) of Swarm Alpha, whereas S_{EW} is the East–West spherical distance, i.e., the distance between adjacent positions (cross-track) of Swarm Alpha and Charlie. Figure 3 shows S_{NS} (left panel) and S_{EW} (right panel) calculated from the positions of Alpha and Charlie between April 2014 and March 2016. Outliers for which the North–South and East–West spherical distances are out of range, namely $S_{\mathrm{NS}} < 110$ km or $S_{\mathrm{NS}} > 120$ km and $S_{\mathrm{EW}} > 200$ km, are removed. In the particular case where Alpha and Charlie are crossing one another and change from ascending to descending orbit tracks, i.e., when $\theta < -87.2°$ or $\theta > 87.2°$, only data points with 4 km $\leq S_{\mathrm{EW}} \leq$ 12 km and are kept.

The model parameters $\mathbf{m}$ are related to the observables $\mathbf{\Gamma}^{(1)}$ resp. $\mathbf{\Gamma}^{(2)}$ as

$$\mathbf{\Gamma}^{(1)} = \mathbf{G}^{(1)}\mathbf{m}, \tag{38}$$

$$\mathbf{\Gamma}^{(2)} = \mathbf{G}^{(2)}\mathbf{m}, \tag{39}$$

with the kernel matrices $\mathbf{G}^{(1)} = \{[\nabla \boldsymbol{G}]_{r\theta}, [\nabla \boldsymbol{G}]_{r\varphi}\}$ and $\mathbf{G}^{(2)} = \{[\nabla \boldsymbol{G}]_{\theta\theta} - [\nabla \boldsymbol{G}]_{\varphi\varphi}, 2[\nabla \boldsymbol{G}]_{\theta\varphi}\}$. $[\nabla \boldsymbol{G}]_{jk}$ (where

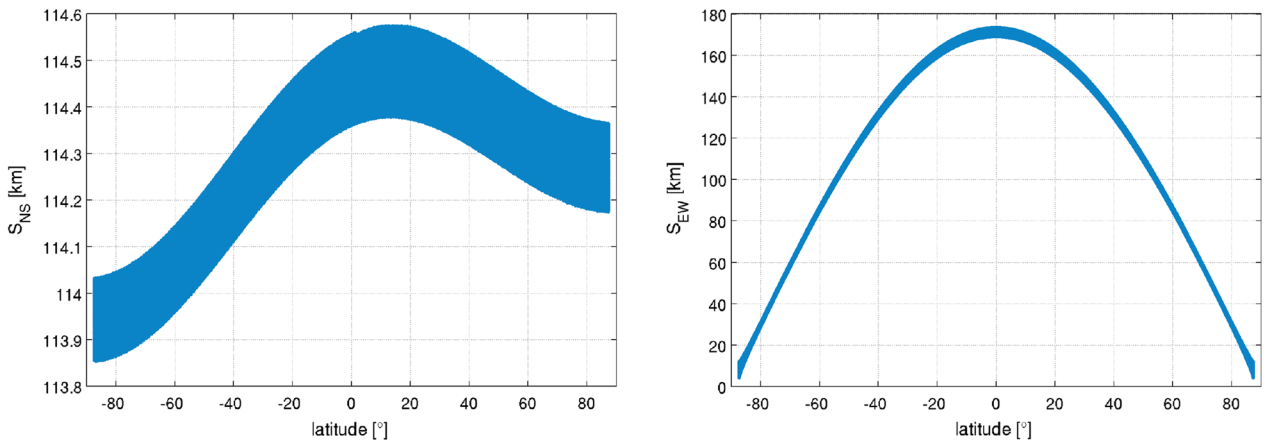

Fig. 3 *Left* North–South spherical distance, S_{NS}, i.e., the distance between consecutive positions (along-track) of Swarm Alpha. *Right* East–West spherical distance, S_{EW}, i.e., the distance between adjacent positions (cross-track) of Swarm Alpha and Charlie. S_{NS} and S_{EW} are calculated based on Swarm Alpha and Charlie positions between April 2014 and March 2016

$j,k = r,\theta,\varphi$) are the individual gradient kernel matrices which can be approximated in a similar fashion to the individual gradient elements $[\nabla \mathbf{B}]_{jk}$ as

$$[\nabla \boldsymbol{G}]_{r\theta} \approx \frac{\mathbf{G}_r(r_1,\theta_1,\varphi_1) - \mathbf{G}_r(r_2,\theta_2,\varphi_2)}{S_{\mathrm{NS}}}, \quad \text{with } \theta_2 - \theta_1 \gg \varphi_2 - \varphi_1, \tag{40}$$

$$[\nabla \boldsymbol{G}]_{r\varphi} \approx \frac{\mathbf{G}_r(r_1,\theta_1,\varphi_1) - \mathbf{G}_r(r_2,\theta_2,\varphi_2)}{S_{\mathrm{EW}}}, \quad \text{with } \varphi_2 - \varphi_1 \gg \theta_2 - \theta_1, \tag{41}$$

$$[\nabla \boldsymbol{G}]_{\theta\theta} \approx \frac{\mathbf{G}_\theta(r_1,\theta_1,\varphi_1) - \mathbf{G}_\theta(r_2,\theta_2,\varphi_2)}{S_{\mathrm{NS}}}, \quad \text{with } \theta_2 - \theta_1 \gg \varphi_2 - \varphi_1, \tag{42}$$

$$[\nabla \boldsymbol{G}]_{\varphi\varphi} \approx \frac{\mathbf{G}_\varphi(r_1,\theta_1,\varphi_1) - \mathbf{G}_\varphi(r_2,\theta_2,\varphi_2)}{S_{\mathrm{EW}}}, \quad \text{with } \varphi_2 - \varphi_1 \gg \theta_2 - \theta_1, \tag{43}$$

$$[\nabla \boldsymbol{G}]_{\theta\varphi} \approx \frac{\mathbf{G}_\theta(r_1,\theta_1,\varphi_1) - \mathbf{G}_\theta(r_2,\theta_2,\varphi_2)}{S_{\mathrm{EW}}}, \quad \text{with } \varphi_2 - \varphi_1 \gg \theta_2 - \theta_1. \tag{44}$$

$\mathbf{G}_r$, $\mathbf{G}_\theta$ and $\mathbf{G}_\varphi$ are the kernel matrices relating the model parameters $\mathbf{m}$ to the field vector components $\mathbf{B_r}$, $\mathbf{B}_\theta$ and $\mathbf{B}_\varphi$ as

$$\mathbf{B_r} = \mathbf{G}_r\mathbf{m}, \tag{45}$$

$$\mathbf{B}_\theta = \mathbf{G}_\theta\mathbf{m}, \tag{46}$$

$$\mathbf{B}_\varphi = \mathbf{G}_\varphi\mathbf{m}. \tag{47}$$

The model parameters $\mathbf{m}$ can be obtained by an iteratively reweighted least-squares approach (Constable 1988; Huber 1964), e.g., in the ith iteration, the model parameters are determined as

$$\mathbf{m}_i = \left[\mathbf{G}^{(\beta)\,T}\mathbf{W}_i\mathbf{G}^{(\beta)}\right]^{-1}\left[\mathbf{G}^{(\beta)\,T}\mathbf{W}_i\right]\mathbf{\Gamma}^{(\beta)}, \tag{48}$$

where the data weight matrix $\mathbf{W}_i$ is updated by the residuals $\mathbf{e} = \mathbf{\Gamma}^{(\beta)} - \mathbf{G}^{(\beta)}\mathbf{m}_{i-1}$ and $\beta = 1,2$. The variance $\tilde{\sigma}^2_{(1)}$ resp. $\tilde{\sigma}^2_{(2)}$ of the estimated model parameters for the observable $\mathbf{\Gamma}^{(1)}$ resp. $\mathbf{\Gamma}^{(2)}$ is

$$\tilde{\sigma}^2_{(1)} = \mathrm{diag}\left[\mathbf{G}^{(1)\,T}\mathbf{W}\mathbf{G}^{(1)}\right]^{-1} \quad \text{resp.} \quad \tilde{\sigma}^2_{(2)} = \mathrm{diag}\left[\mathbf{G}^{(2)\,T}\mathbf{W}\mathbf{G}^{(2)}\right]^{-1} \tag{49, 50}$$

The selected Swarm data (Alpha and Charlie positions) have been used to approximate the kernel matrices $\mathbf{G}^{(1)}$ and $\mathbf{G}^{(2)}$ and compute the variances $\tilde{\sigma}^2_{(1)}$ and $\tilde{\sigma}^2_{(2)}$ which are shown in Fig. 4a, b in dependence of degree n and order m. In addition, $\tilde{\sigma}^2_{(0)} = \mathrm{diag}\left[\mathbf{G}^{(0)\,T}\mathbf{W}\mathbf{G}^{(0)}\right]^{-1}$, which is the model variance for the observable $\mathbf{\Gamma}^{(0)} = \{[\nabla \mathbf{B}]_{rr}\}$, is computed by evaluating the theoretical kernel matrix $\mathbf{G}^{(0)}$ at Alpha positions. $\mathbf{G}^{(0)}$ relates the model parameters $\mathbf{m}$ to the radial gradient $[\nabla \mathbf{B}]_{rr}$ as

$$[\nabla \mathbf{B}]_{rr} = \mathbf{G}^{(0)}\mathbf{m}, \tag{51}$$

and can easily be constructed by looking at Eqs. (2) and (3). $\tilde{\sigma}^2_{(0)}$ is shown in Fig. 4c. The approximated model variances $\tilde{\sigma}^2_{(1)}$ and $\tilde{\sigma}^2_{(2)}$ for the observables $\mathbf{\Gamma}^{(1)}$ and $\mathbf{\Gamma}^{(2)}$ bear a good resemblance and are very similar to the calculated theoretical variance $\tilde{\sigma}^2_{(0)}$ which corresponds to the observable $\mathbf{\Gamma}^{(0)}$. Therefore, $\mathbf{\Gamma}^{(1)}$ and $\mathbf{\Gamma}^{(2)}$, which are approximated based on Swarm Alpha and Charlie data, carry similar information content (regarding the estimation of the model parameters) to the (ideal) radial gradient ($\mathbf{\Gamma}^{(0)}$), which is not possible to be measured or estimated directly from the Swarm configuration. $\tilde{\sigma}^2_{(2)}$ shows some instabilities in the zonal terms ($m = 0$), which is most probably due to the Swarm orbit and in particular the polar gap in combination with the sensitivity of $\mathbf{\Gamma}^{(2)}$ to the East–West gradients $[\nabla \mathbf{B}]_{\theta\varphi}$, $[\nabla \mathbf{B}]_{\varphi\varphi}$, which do not constrain the zonal terms sufficiently (Kotsiaros and Olsen 2012). A quantitative comparison between $\tilde{\sigma}^2_{(0)}$, $\tilde{\sigma}^2_{(1)}$ and $\tilde{\sigma}^2_{(2)}$ with the analytically calculated theoretical variances $\sigma^2_{(0)}$, $\sigma^2_{(1)}$ and $\sigma^2_{(2)}$ shown in Fig. 2 cannot be made since the scales are so different. However, one recognizes similar features appearing in the same degree ranges for $\tilde{\sigma}^2_{(0)}$, $\tilde{\sigma}^2_{(1)}$, $\tilde{\sigma}^2_{(2)}$ and $\sigma^2_{(0)}$, resp. $\sigma^2_{(1)}$, resp. $\sigma^2_{(2)}$. Notice, for example, the relatively lower variances at degrees $n \approx 10 - 40$ in both cases. This band of lower variances (higher information) is relative to the satellite altitude. In particular, lower altitude expands this band to higher degrees. In case of $\tilde{\sigma}^2_{(0)}$, $\tilde{\sigma}^2_{(1)}$ and $\tilde{\sigma}^2_{(2)}$, there seems to be, in addition to degree n, a dependence on the order m, which is more prominent for $\tilde{\sigma}^2_{(2)}$. This is attributed to the non-perfect distribution of Swarm Alpha and Charlie data on the contrary to the theoretical case where perfect data distribution is assumed.

Lithospheric field models are derived from the pseudo-radial gradients $\mathbf{\Gamma}^{(1)}$ and $\mathbf{\Gamma}^{(2)}$, which are estimated from the selected Swarm Alpha and Charlie data. The radial component of the lithospheric field resulting from the model obtained by $\mathbf{\Gamma}^{(1)}$ resp. $\mathbf{\Gamma}^{(2)}$ is shown in Fig. 5a resp. Fig. 5b. For reference, the radial lithospheric field resulting from MF7 and CM5 (Sabaka et al. 2015) is also shown in Fig. 5c resp. Fig. 5d. The fields are calculated at the Earth's surface from coefficients of degrees $16 \leq n \leq 90$. Green lines indicate the boundaries of the major tectonic plates, whereas red lines locate the dip equator (0° QD latitude) and ±55° iso-QD latitudes. The model obtained

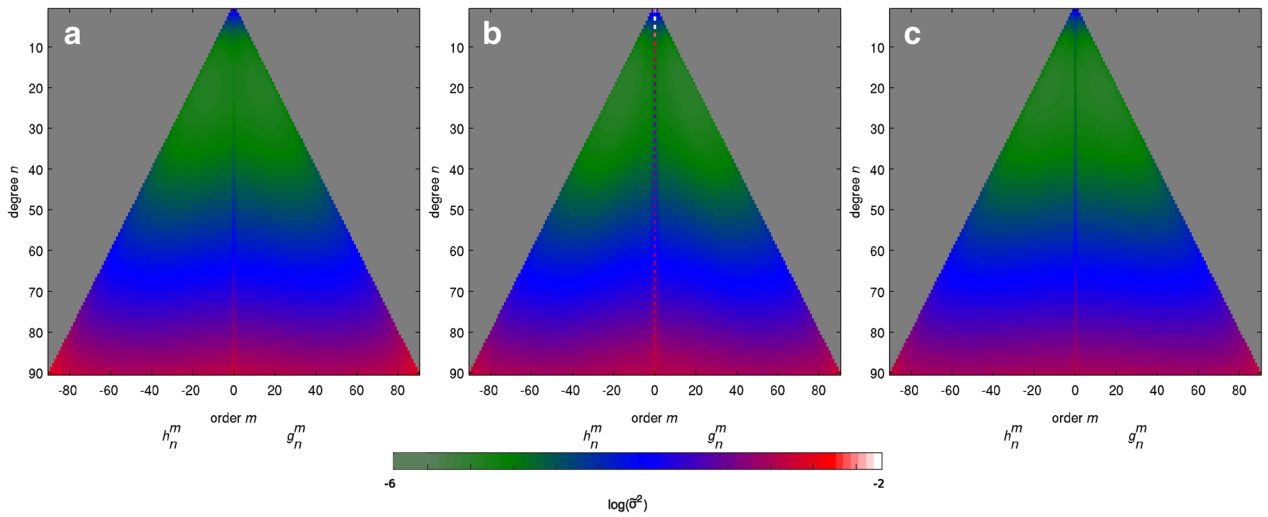

Fig. 4 Variances $\tilde{\sigma}^2_{(1)}$ (a) and $\tilde{\sigma}^2_{(2)}$ (b) computed from the approximated kernel matrices $\mathbf{G}^{(1)}$ resp. $\mathbf{G}^{(2)}$. Variance $\tilde{\sigma}^2_{(0)}$ (c) computed from the theoretical kernel matrix $\mathbf{G}^{(0)}$. The variances are calculated based on Swarm Alpha and Charlie positions between April 2014 and March 2016

by the pseudo-radial gradient $\mathbf{\Gamma}^{(2)}$ seems to be dominated by a strong signal at QD latitudes polewards of $\pm 55°$ which also leaks to lower latitudes. Remember that $\mathbf{\Gamma}^{(2)}$ is built exclusively from gradients of the horizontal components, $[\nabla \mathbf{B}]_{\theta\theta}$, $[\nabla \mathbf{B}]_{\varphi\varphi}$ and $[\nabla \mathbf{B}]_{\theta\varphi}$ (and therefore horizontal components cannot be excluded from QD latitudes polewards of $\pm 55°$ otherwise we would end up with no data in those regions), which are sensitive to disturbing effects due to electrical currents of ionospheric/magnetospheric origin, such as field aligned currents. Therefore, if $\mathbf{\Gamma}^{(2)}$ is to be used for lithospheric field modeling, it is recommended that $\mathbf{\Gamma}^{(2)}$ is excluded in the regions polewards of $\pm 55°$ QD latitude and data of the radial vector and/or gradients of the radial vector and/or scalar data are used instead. In the following, we will concentrate on the model retrieved from $\mathbf{\Gamma}^{(1)}$ (Fig. 5a), which from now on will be called $\mathrm{SM}_{\Gamma^{(1)}}$ (Swarm Model). This model exhibits a stronger signal over the oceanic regions and the regions associated with the magnetic lineations that arise from the seafloor spreading. Moreover, it exhibits sharper lithospheric field features, which is a characteristic property of the radial gradient, compared to MF7 and CM5. Note, for example, the crisp definition of the features in the polar regions, northwest Africa and the Bangui anomaly.

In a similar fashion to $\mathrm{SM}_{\Gamma^{(1)}}$, five additional models are obtained for comparison by vector data as well as by North–South and East–West gradient estimates. Specifically, the following models are derived

- SM_{v} model derived by vector data from Swarm Alpha.
- $\mathrm{SM}_{\mathrm{vNS}}$ model derived by Swarm Alpha vector data and North–South gradients estimated from Swarm Alpha vector data, see Eqs. (33) and (35).
- $\mathrm{SM}_{\mathrm{vEW}}$ model derived by Swarm Alpha vector data and East–West gradients estimated from Swarm Alpha and Charlie vector data, see Eqs. (34), (36) and (37).
- $\mathrm{SM}_{\mathrm{vNSEW}}$ model derived by Swarm Alpha vector, North–South and East–West gradients estimated from Swarm Alpha and Charlie vector data. For this model, North–South and East–West gradients (as well as their associated kernel matrices) are approximated by simple first differences (no division with the spherical distance), in a similar fashion to how the gradients are commonly treated for modeling, see, for example, Finlay et al. (2016), Olsen et al. (2015), Olsen et al. (2016), Sabaka et al. (2015) .
- $\mathrm{SM}_{\Gamma^{(1)}_\delta}$ this model is equivalent to $\mathrm{SM}_{\Gamma^{(1)}}$ except that the gradients involved in $\mathbf{\Gamma}^{(1)}$ (and the associated gradient kernel matrices) are approximated by simple data differences (no division with the spherical distance).

No special data filtering nor regularization has been applied in $\mathrm{SM}_{\Gamma^{(1)}}$ or in any of the additional models as opposed to CM5 where regularization is applied above degree $n = 60$ (Sabaka et al. 2015) and MF7 where data filtering and line leveling is applied to the data (Maus et al. 2008).

Figure 6a shows Mauersberger–Lowes spectra of the lithospheric field models SM_{v}, $\mathrm{SM}_{\mathrm{vNS}}$, $\mathrm{SM}_{\mathrm{vEW}}$, $\mathrm{SM}_{\mathrm{vNSEW}}$, $\mathrm{SM}_{\Gamma^{(1)}}$ and $\mathrm{SM}_{\Gamma^{(1)}_\delta}$. For reference, the power spectra of

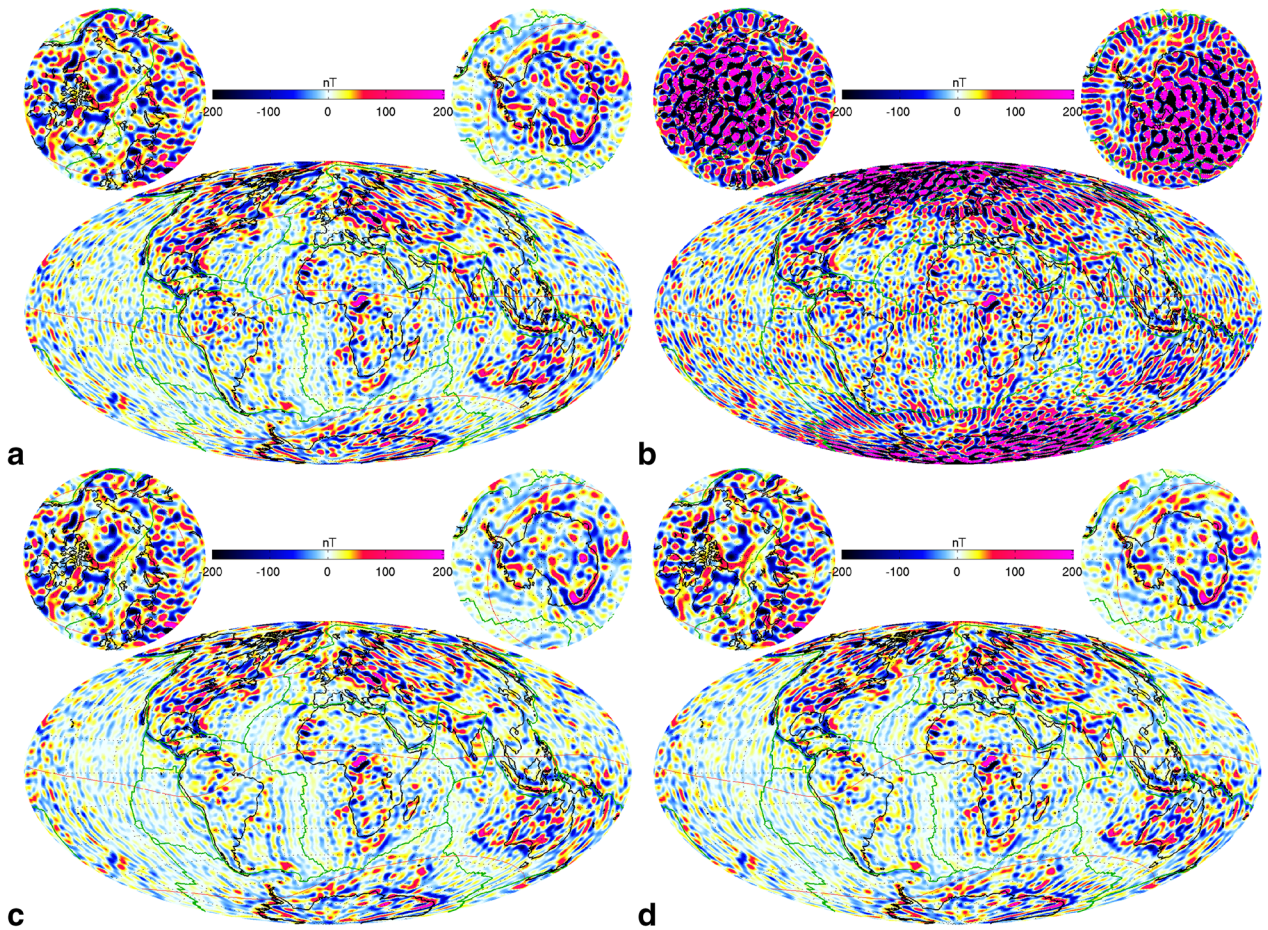

Fig. 5 Maps of radial lithospheric field calculated at the Earth's surface from coefficients of degrees $16 \leq n \leq 90$ taken from the field model derived from $\mathbf{\Gamma}^{(1)}$ (**a**) and $\mathbf{\Gamma}^{(2)}$ (**b**). For reference, the radial lithospheric field at the Earth's surface from coefficients of degrees $16 \leq n \leq 90$ taken from MF7 (**c**) and CM5 (**d**) is also shown. *Green lines* indicate the boundaries of the major tectonic plates, whereas *red lines* locate the dip equator (0° QD latitude) and ±55° iso-QD latitudes

MF7 and CM5 are also presented. Up to degree $n \approx 40$, all derived models agree relatively well with MF7 and CM5, whereas above that degree, SM_v, SM_{vNS} and SM_{vEW} have considerably more power. On the other hand, SM_{vNSEW}, $SM_{\Gamma^{(1)}}$ and $SM_{\Gamma^{(1)}_\delta}$ follow the power of MF7 and CM5 up to degree $n = 83$ where they start to deviate. Looking at the spectra of model differences (dashed lines in Fig. 6a) and the degree correlation, ρ_n, cf. Langel and Hinze (1998), Fig. 6b, $SM_{\Gamma^{(1)}_\delta}$ and SM_{vNSEW} are very similar and agree better with MF7 and CM5 than $SM_{\Gamma^{(1)}}$.

Figure 7a–f resp. 7g–l presents the relative difference (in %) between each coefficient of the various derived models and MF7 resp. CM5 in a degree versus order matrix. The model SM_v, built only from vector data, shows significant differences with respect to MF7 and CM5 after degree $n \approx 55$. Inclusion of North–South gradients in the SM_{vNS} improves the agreement in the high-degree near-zonal coefficients ($|m| \approx 0 \ll n$), whereas inclusion of East–West gradients in the SM_{vEW} improves the agreement in the near-sectoral terms ($|m| \approx n \gg 0$). The model SM_{vNSEW}, built including both North–South and East–West gradients, improves the determination of both the near-zonal and near-sectoral terms leading to an overall improved model. The model $SM_{\Gamma^{(1)}}$, which is built exclusively from pseudo-radial gradient $\mathbf{\Gamma}^{(1)}$, results in better agreement with MF7 and CM5 than SM_{vNSEW} in the high-degree zonal coefficients ($m = 0$). However, the high-degree near-sectoral ($|m| \approx n \gg 0$) coefficients show a worse agreement. This is not the case if we look at $SM_{\Gamma^{(1)}_\delta}$ which is also derived, similarly to $SM_{\Gamma^{(1)}}$, exclusively from $\mathbf{\Gamma}^{(1)}$ but gradients are estimated by simple data differences instead of dividing by the spherical distance. The agreement of $SM_{\Gamma^{(1)}_\delta}$ with MF7 resp. CM5 is generally on the same level as SM_{vNSEW} and improved in the zonal terms.

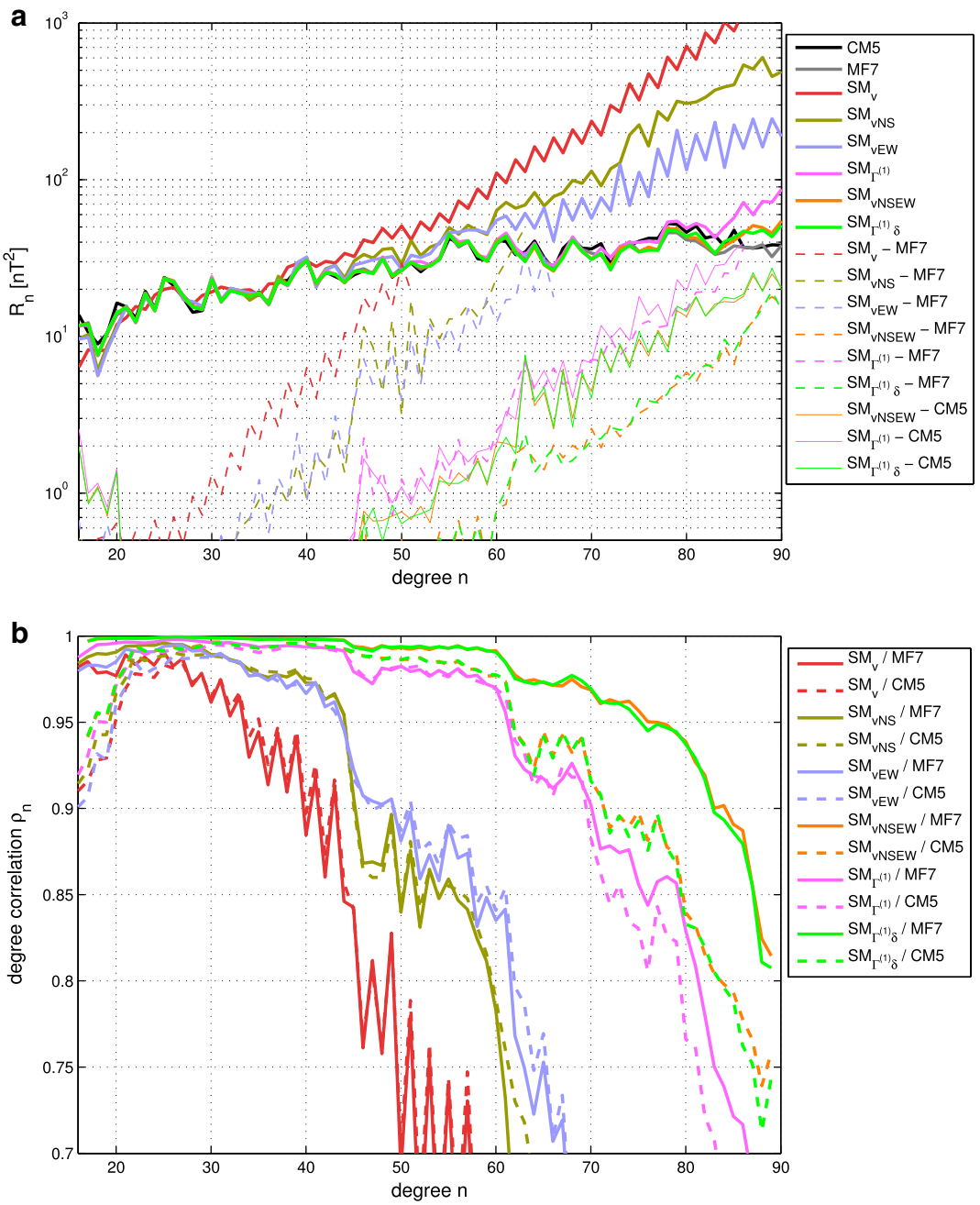

Fig. 6 **a** Power spectra of the lithospheric field ($n = 16$–90) from all derived models at the Earth's surface. Spectra of models are shown in *solid lines*, spectra of differences between models in *dashed lines*. **b** Degree correlations of the models with respect to MF7 and CM5

Maps of lithospheric field differences of B_r between MF7 and SM_{vNSEW} (a), $SM_{\Gamma^{(1)}}$ (b) and $SM_{\Gamma^{(1)}\delta}$ (c) as well as between CM5 and SM_{vNSEW} (d), $SM_{\Gamma^{(1)}}$ (e) and $SM_{\Gamma^{(1)}\delta}$ (f) are shown in Fig. 8. The maps are produced at the Earth's surface using degrees $n = 16$–70 of the respective models. Overall, the agreement of the derived models with MF7 is slightly better than with CM5. In particular, $SM_{\Gamma^{(1)}}$ shows slightly higher differences with MF7 and CM5 than SM_{vNSEW} or $SM_{\Gamma^{(1)}\delta}$, whereas the differences of SM_{vNSEW} and $SM_{\Gamma^{(1)}\delta}$ with both MF7 and CM5 are very similar. On the other hand, compared to SM_{vNSEW}, the models $SM_{\Gamma^{(1)}}$ and $SM_{\Gamma^{(1)}\delta}$ show a relatively good agreement with MF7 and CM5 at the poles despite the fact that the polar gap is not accounted for as opposed to

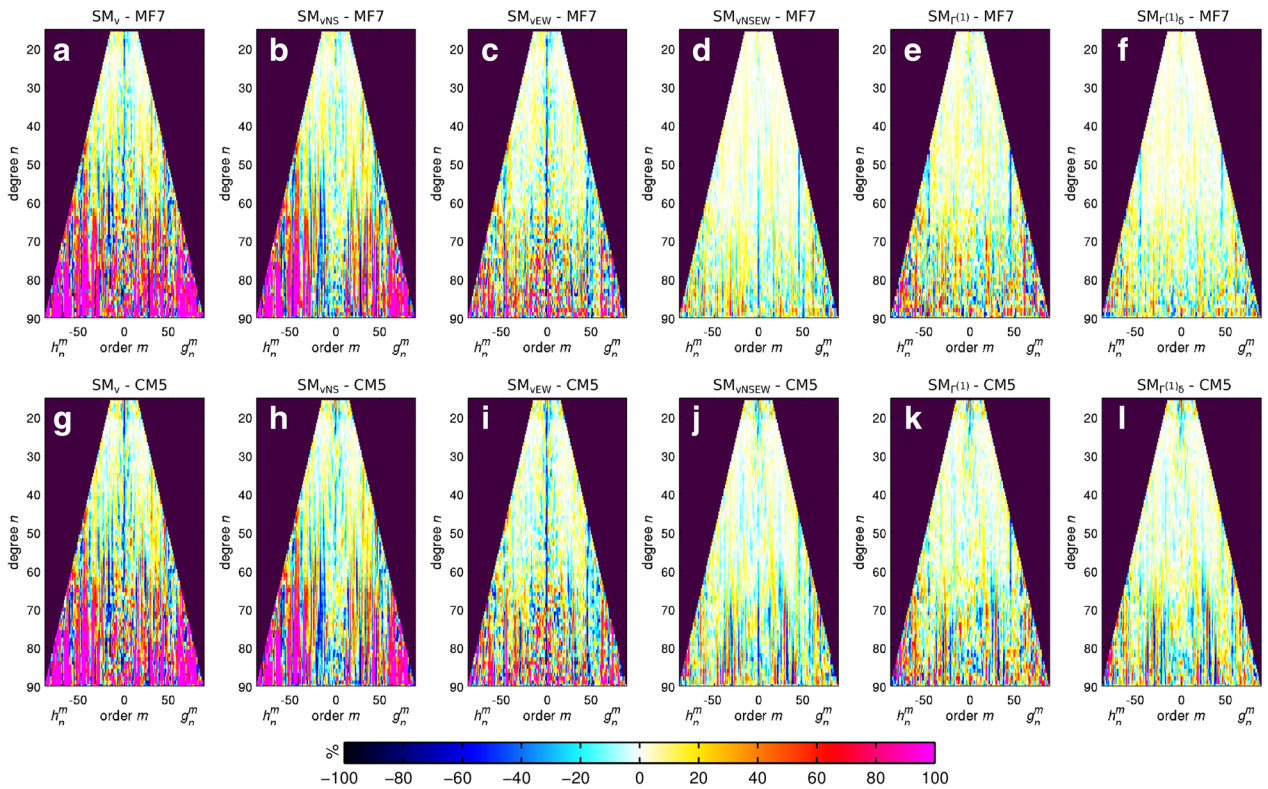

Fig. 7 Sensitivity matrices—relative difference (in %) between each coefficient of the derived models SM$_v$, SM$_{vNS}$, SM$_{vEW}$, SM$_{vNSEW}$, SM$_{\Gamma^{(1)}}$, SM$_{\Gamma^{(1)}_\delta}$ and MF7 (**a**–**f**) resp. CM5 (**g**–**l**) in a degree versus order matrix

MF7 and CM5. In MF7, the polar gap is filled with synthetic model values from MF5 (Maus et al. 2007) and in CM5 the lithospheric field is smoothened over the polar gap region above degree $n = 60$ (Sabaka et al. 2015). Despite leaving the polar gap untreated in SM$_{\Gamma^{(1)}}$ and SM$_{\Gamma^{(1)}_\delta}$, no particular ringing appears which is usually the case if the polar gaps are not accounted for (Sabaka et al. 2015; Maus et al. 2008).

Conclusions

It has been shown that the gradient combinations $\mathbf{\Gamma}^{(1)} = \{[\nabla\mathbf{B}]_{r\theta}, [\nabla\mathbf{B}]_{r\varphi}\}$ and $\mathbf{\Gamma}^{(2)} = \{[\nabla\mathbf{B}]_{\theta\theta} - [\nabla\mathbf{B}]_{\varphi\varphi}, 2[\nabla\mathbf{B}]_{\theta\varphi}\}$ produce similar signal content as the radial gradient $\mathbf{\Gamma}^{(0)} = \{[\nabla\mathbf{B}]_{rr}\}$. That is a general theoretical conclusion from special tensorial analysis of potential fields and has been already shown for the gravity potential by Rummel and van Gelderen (1992). For the geomagnetic case, this has important implications because the gradients of the field are not measured instantaneously by a single satellite instrument. The radial gradient is currently not possible to be measured, as, for example, in the gravity case and the GOCE mission where the complete gradient tensor can be determined instantaneously by a gravity gradiometer (Rummel et al. 2011). Nevertheless, contrary to the radial gradient $\{[\nabla\mathbf{B}]_{rr}\}$, which is not possible to be measured with the Swarm configuration, the gradient combinations $\{[\nabla\mathbf{B}]_{r\theta}, [\nabla\mathbf{B}]_{r\varphi}\}$ and $\{[\nabla\mathbf{B}]_{\theta\theta} - [\nabla\mathbf{B}]_{\varphi\varphi}, 2[\nabla\mathbf{B}]_{\theta\varphi}\}$ can be determined by the lowest satellite pair and contain similar information regarding the estimation of the model parameters as the radial gradient. Furthermore, the gradient combinations can be related to the magnetic field potential and the traditional spherical harmonic expansion coefficients with the help of simple eigenvalue relations, and therefore, they can be used for magnetic field modeling. For the first time, magnetic field models are derived exclusively from estimated gradient observations as opposed to the standard technique of using a combination of vector and estimated gradients (Finlay et al. 2016; Olsen et al. 2015, 2016; Sabaka et al. 2015). Moreover, one of the main models (SM$_{\Gamma^{(1)}}$) presented here is built by gradient estimates using first-order Taylor approximation (dividing by the spherical distance), on the contrary to the standard approach of estimating gradients simply with vector differences (Kotsiaros et al. 2015). It seems that when gradients are estimated by simple data differences, such as the model SM$_{\Gamma^{(1)}_\delta}$ presented here, instead of dividing by the spherical distance, the derived models are slightly improved. The models are derived using 23 months of Swarm data with a sampling

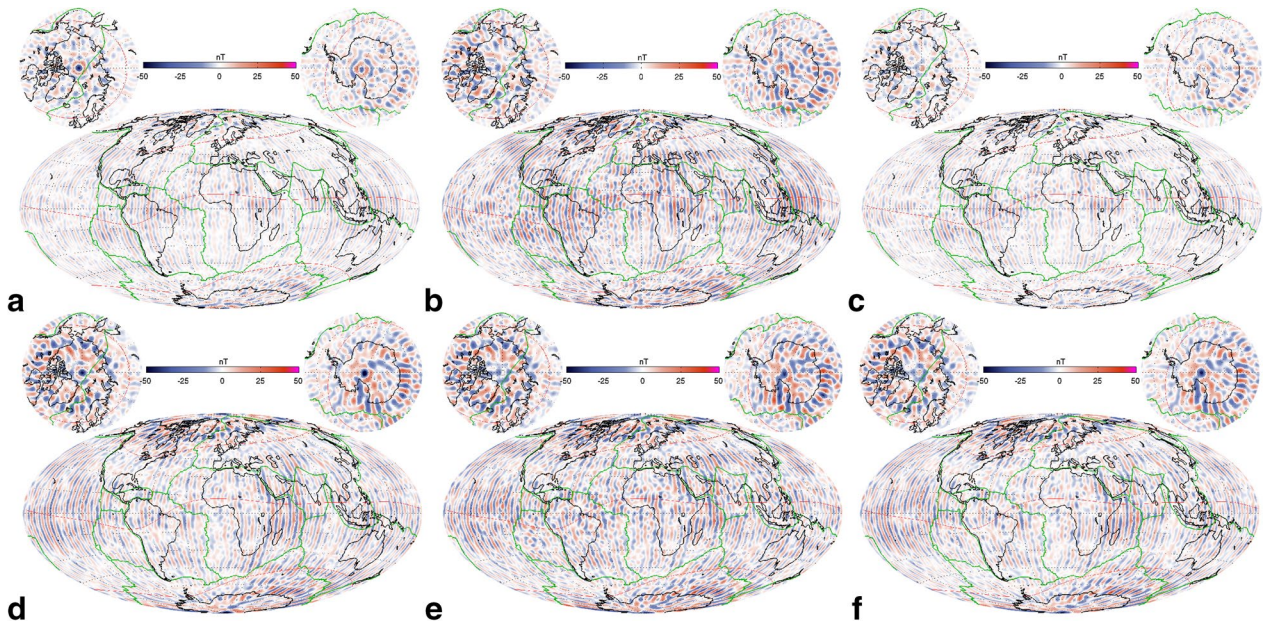

Fig. 8 Maps of radial lithospheric field differences calculated at the Earth's surface from coefficients of degrees $16 \leq n \leq 70$ between $SM_{\nu NSEW}$, $SM_{\Gamma^{(1)}}$, $SM_{\Gamma^{(1)}\delta}$ and MF7 (**a**–**c**) resp. CM5 (**d**–**f**)

rate of 15 seconds. Tests have also been performed deriving equivalent models to the ones presented here using 5 s sampling rate, but no particular improvements were detected. The pseudo-radial gradient $\mathbf{\Gamma}^{(1)} = \{[\nabla \mathbf{B}]_{r\theta}, [\nabla \mathbf{B}]_{r\varphi}\}$, estimated with simple vector differences, leads to a very similar lithospheric model to the model retrieved by using approximately three times more data, i.e. a full set of vector, North–South and East–West gradients. This demonstrates the high information content of $\mathbf{\Gamma}^{(1)}$. Moreover, despite not accounting for the polar gaps, models resulting from $\mathbf{\Gamma}^{(1)}$ do not suffer from ringing and seem to agree better in the polar gap regions to the reference models MF7 and CM5 than the model built from the full set of vector, North–South and East–West gradients.

In this paper, the performance of lithospheric field models, such as the $SM_{\Gamma^{(1)}}$ determined exclusively by gradient combinations has been studied in detail. However, tests have also been performed extending the $SM_{\Gamma^{(1)}}$ to include the static main field (degrees $n = 1$–15). The extended $SM_{\Gamma^{(1)}}$ is derived in a similar fashion to $SM_{\Gamma^{(1)}}$, which is presented here, except that model predictions of the core field are not subtracted from the Swarm data. The initial tests show that, similarly to the lithospheric field case, $\mathbf{\Gamma}^{(1)}$ can lead to high-quality models also for the static part of the core field. Further tests regarding the performance of $\mathbf{\Gamma}^{(1)}$ on the determination of the static core field as well as its time-dependent part can be an extension to the current work and the topic of a separate paper.

Acknowledgements
The author would like to thank ESA STSE Changing Earth Science Network for financing the SGC project, within the framework of which this work was completed. The author also wishes to express his gratitude to Rainer Rummel for his ideas on tensorial analysis and for providing influential motivation in the realization of this work. Chris Finlay and Nils Olsen are also thanked for their support and for the helpful discussions on the various aspects of geomagnetic field modeling. Terry Sabaka is thanked for providing CM5 model.

Received: 31 December 2015 Accepted: 27 June 2016
Published online: 22 July 2016

References

Backus G, Parker R, Constable C (1996) Foundations of geomagnetism. Cambridge University Press, Cambridge
Constable CG (1988) Parameter estimation in non-Gaussian noise. Geophys J 94:131–142
Finlay CC, Olsen N, Kotsiaros S, Gillet N, Tøffner-Clausen L (2016) Recent geomagnetic secular variation from Swarm and ground observatories in the CHAOS-6 geomagnetic fieldmodel. Earth Planets Space. doi:10.1186/s40623-016-0486-1
Friis-Christensen E, Lühr H, Hulot G (2006) Swarm: a constellation to study the Earth's magnetic field. Earth Planets Space 58(4):351–358
Groten E, Moritz H, P. Ohio State University. Institute of Geodesy, Cartography, and A. F. C. R. L. (U.S.) (1964) On the accuracy of Geoid heights and deflections of the vertical, report (Ohio State University. Institute of Geodesy, Photogrammetry and Cartography), Ohio State University Research Foundation
Huber PJ (1964) Robust estimation of a location parameter. Ann Math Stat 35(1):73–101. doi:10.1214/aoms/1177703732
Kotsiaros S, Finlay C, Olsen N (2015) Use of along-track magnetic field differences in lithospheric field modelling. Geophys J Int 200(2):878–887
Kotsiaros S, Olsen N (2012) The geomagnetic field gradient tensor. GEM Int J Geomath 3:297–314. doi:10.1007/s13137-012-0041-6
Langel RA (1987) The main field. In: Jacobs JA (ed) Geomagnetism, vol 1. Academic Press, London, pp 249–512

Langel RA, Hinze W (1998) he magnetic field of the Earth's lithosphere. The satellite perspective. Cambridge University Press, Cambridge, pp 113–122
Lowes FJ (1966) Mean-square values on sphere of spherical harmonic vector fields. J Geophys Res 71:2179
Lowes FJ (1974) Spatial power spectrum of the main geomagnetic field, and extrapolation to the core. Geophys J R Astr Soc 36:717–730
Maus S, Lühr H, Rother M, Hemant K, Balasis G, Ritter P, Stolle C (2007) Fifth-generation lithospheric magnetic field model from CHAMP satellite measurements. Geochem Geophys Geosyst 8(5):Q05,013
Maus S, Yin F, Lühr H, Manoj C, Rother M, Rauberg J, Michaelis I, Stolle C, Müller R (2008) Resolution of direction of oceanic magnetic lineations by the sixth-generation lithospheric magnetic field model from CHAMP satellite magnetic measurements. Geochem Geophys Geosyst 9(7):Q07,021
Meissl P (1971) A study of covariance functions related to the Earth's disturbing potential. Ohio State Univ Columbus Dept of Geodetic Science, report No. 151
Neubert T et al (2001) Ørsted satellite captures high-precision geomagnetic field data. Eos Trans AGU 82(7):81–88
Olsen N et al (2015) The swarm initial field model for the 2014 geomagnetic field. Geophys Res Lett 42(4):2014GL062,659
Olsen N, Finlay CC, Kotsiaros S, Tøffner-Clausen L (2016) A model of earth's magnetic field derived from two years of swarm satellite constellation data. EPS (accepted)
Reigber C, Lühr H, Schwintzer P, Wickert J (2005) Earth observation with CHAMP: results from three years in orbit. Springer, Berlin
Richmond AD (1995) Ionospheric electrodynamics using magnetic apex coordinates. J Geomagn Geoelectr 47:191–212
Rummel R (1997) Spherical properties of the earth's gravitational potential and its first and second derivatives. Lecture Notes in Earth Sciences. Springer, Berlin 65:359–404. doi:10.1007/BFb0011699
Rummel R, Yi W, Stummer C (2011) Goce gravitational gradiometry. J Geod 85(11):777–790. doi:10.1007/s00190-011-0500-0
Rummel R, van Gelderen M (1992) Spectral analysis of the full gravity tensor. Geophys J Int 111(1):159–169
Sabaka TJ, Olsen N, Tyler RH, Kuvshinov A (2015) CM5, a pre-Swarm comprehensive magnetic field model derived from over 12 years of CHAMP, Ørsted, SAC-C and observatory data. Geophys J Int 200:1596
van Gelderen M, Koop R (1997) The use of degree variances in satellite gradiometry. J Geod 71(6):337–343
Zerilli JF (1970) Tensor harmonics in canonical form for gravitational radiation and other applications. J Math Phys 11(7):2203–2208. doi:10.1063/1.1665380